

Whisker & Hillock Formation on Sn, Sn-Cu and Sn-Pb Electrodeposits

W. J. Boettinger*, C. E. Johnson, L. A. Bendersky, K.-W. Moon,

M. E. Williams and G. R. Stafford

Metallurgy Division

NIST

Gaithersburg, MD 20899

Thursday, March 03, 2005

Abstract

High purity bright Sn, Sn-Cu and Sn-Pb layers, 3, 7 and 16 μm thick were electrodeposited on phosphor bronze cantilever beams in a rotating disk apparatus. Beam deflection measurements within 15 min of plating proved that all electrodeposits had in-plane compressive stress. In several days, Sn-Cu deposits, which have the highest compressive stress, develop 50 μm contorted hillocks and 200 μm whiskers, pure Sn deposits develop 20 μm compact conical hillocks, and Sn-Pb deposits, which have the lowest compressive stress, remain unchanged. The initial compressive stresses for the alloys compared to that of pure Sn can be understood in terms of the precipitation of Cu_6Sn_5 or Pb particles within supersaturated Sn grains shortly after plating. Over time, beam deflection is due to creep of the electrodeposit and the formation of Cu_6Sn_5 on the bronze/Sn interface that respectively decrease and slightly increase the compressive stress in the deposit. Uniform creep occurs for Sn-Pb because it has an equiaxed grain structure. Localized creep in the form of hillocks and whiskers occurs for Sn and Sn-Cu because both have columnar structures. Compact hillocks form for the Sn deposits because the columnar grain boundaries are mobile. Contorted hillocks and whiskers form for the Sn-Cu deposits because the columnar grain boundary motion is impeded.

Key Words: whiskers, electroplating, creep, grain boundary diffusion, solder.

* email: william.boettinger@nist.gov

1. Introduction

Sn whiskers have been an industrial concern and interesting problem for many years. They are known to cause short circuits in fine pitch pretinned electrical components. In contrast to many whisker growth processes, Sn whiskers grow by the addition of material at their base not at their tip; i.e., they grow out of the substrate [1]. They can grow from as-formed electrodeposits, vapor deposited material [2] and intentionally deformed coatings of Sn [3]. Similar whiskers are observed in Cd, In and Zn. Whiskers appear to be a local response to the existence of residual stress. *Compressive* residual stress is usually considered a precondition for whisker growth [3]. Annealing or melting (*reflow* in solder terminology) usually mitigates the growth. In 1966, Pb additions of a few percent to Sn electroplate were found to greatly reduce the tendency to form whiskers [4] and interest in the subject waned. Recently, interest in Pb-free surface finishes for *green* manufacturing of electronic components has reopened this dormant field and an annotated bibliography has been prepared [5]. Questions remain as to the dominant source of stress and the precise growth mechanism. The final goal is the development of a practical mitigation strategy for electronic components during electroplating, storage and/or service.

In a subject related to whisker growth, there is an extensive literature that treats the growth of hillocks on thin films often made from the vapor phase where compressive stress may be due to differential thermal contraction of the deposit and substrate during cooling from deposition temperature (for example: [6, 7, 8]). In contrast to Sn whiskers, hillock protrusions from the surface usually have aspect ratios near unity. Hillock growth is often treated as a localized diffusional creep/grain boundary sliding phenomenon. However because Sn electroplating is performed at room temperature, residual stresses can not have a thermal origin. One of the

most commonly discussed sources of compressive stress in Sn electrodeposits is intermetallic (IMC) formation due to the reaction of Sn with Cu in the substrate metal [9, 10, 11].

In a previous paper [12], it was shown that filamentary whisker defects were not observed on pure bright Sn electrodeposits if high purity (18 M Ω -cm) water was used to prepare the commercial methanesulfonate electrolyte. Intentional Cu additions as an impurity to the electrolyte in the range from 0.5×10^{-3} mol/L to 25×10^{-3} mol/L did however cause whiskers and hillocks to form over a period of 24 days with defect densities ranging from 33 mm⁻² to 100 mm⁻². But IMC forms on the interface between the deposit and the substrate in both cases. Thus we questioned whether it was the major stress source for whisker formation, especially because electroplating itself often produces significant residual stress in deposits [13].

Using deflection measurements of plated cantilever beams, the present paper seeks to determine whether the in-plane residual stress in Sn-Cu electrodeposits is compressive and greater than that for pure Sn electrodeposits. Sn-Pb alloys were included in the study because of the known whisker mitigation effect of Pb. The paper also determines the relative amounts of stress generated by the electrodeposition process, the alloy additions and how the reaction at the deposit/substrate boundary changes the deposit stress with time. The paper reports the propensity for whisker/hillock formation and the interior microstructure of the electrodeposits and compares this tendency with the stress and plastic strain rate of the deposits. Finally a mechanism based on localized creep of columnar grain structures is suggested for the localized surface disturbance in response to the compressive stress.

2. Reaction of Sn with Cu

Because of its reported role in whisker growth, a preliminary point is usefully discussed here. The formation of the layer of Cu_6Sn_5 by reaction between Cu and a layer of Sn is a relatively slow process controlled by diffusion. Onishi & Fujibuchi [14] measured the intermetallic growth rates in diffusion couples between Cu and Sn between 109 °C and 220 °C. The thickness of the total intermetallic layer ($\text{Cu}_6\text{Sn}_5 + \text{Cu}_3\text{Sn}$) is given by

$$d_{IMC} = \sqrt{Bt} \quad [1]$$

with $B = 6.23 \times 10^{-6} \exp(Q/RT) \text{ cm}^2/\text{s}$ and $Q = 57.7 \text{ kJ/mol}$. At 298 K, the extrapolated value of B is $4.7 \times 10^{-16} \text{ cm}^2/\text{s}$. A square root of time dependence is valid as long as the intermetallic layer is much thinner than the Sn and Cu layers. Alternately Tu and Thompson [15] have measured the growth rate of intermetallic at room temperature. They observed only Cu_6Sn_5 and obtained

$$d_{IMC} = B't \quad [2]$$

with $B' = 4 \times 10^{-12} \text{ cm/s}$ for IMC thicknesses up to 300 nm. This linear form implies that interface attachment kinetics is dominant for room temperature IMC growth, not diffusion, at least in its initial stage. Finally, in unpublished work [16] using Sn plating on a Cu metallized quartz crystal resonator and stripping after different hold times, the intermetallic was found to grow as \sqrt{Bt} at room temperature with $B = 1.76 \times 10^{-15} \text{ cm}^2/\text{s}$. Below, we present measurements of residual stress in deposits 15 minutes after plating. The above considerations indicate that less than 20 nm of intermetallic can form during this time and would have negligible effect on the stress in 3 to 16 μm thick deposits. On the other hand, the above suggests that between 1.2 μm and 2.3 μm may form in a year ($3 \times 10^7 \text{ s}$) and the stress of the deposit may be influenced at longer times.

For pure Sn in contact with a Cu substrate, we do not expect, nor has it ever been observed to our knowledge, that discrete (isolated) intermetallic particles form on Sn grain boundaries due to rapid diffusion of Cu from the substrate. Thus we will only consider the effect of (nearly) planar layers of IMC forming at the Cu/Sn interface. The supersaturation required to nucleate a discrete IMC particle could only occur during the short period of time before a continuous layer of the same IMC coats the Cu/Sn interface. After that time, formation and/or further growth of discrete IMC particles on grain boundaries is not possible. Similarly we have not observed rapid penetration of IMC along Sn grain boundaries. However as shown below, when Cu^{2+} is present in the electrolyte, discrete IMC particles can form within the Sn grains by solid state precipitation from a Cu supersaturated Sn solid solution formed by electrochemical codeposition.

3. Experimental Method

Using a metal shear, coupons, 2.5 cm square, were cut from 152 μm thick, half hard, rolled phosphor bronze with nominal mass fractions of Cu-5 % Sn-(0.03 to 0.35) %P. The edges were deburred with a jeweler's file and the surface to be plated was polished with 3 μm Al_2O_3 . Using the geometry shown in Fig. 1, cantilever beams, 2mm by 20mm, and a supporting frame were chemically etched from the coupons using acid resistant tape and 60% nitric acid. It was found necessary to employ beams perpendicular to the sheet rolling direction to obtain reproducible beam deflections after plating. This may lead to a nonisotropic biaxial response of the beams, but this factor will be ignored.

Prior to electroplating, all substrates were immersed in 25 % sulfuric acid solution for 5 s to remove oxide and were rinsed in deionized water. Bright electrodeposits of Sn, Sn-Cu and Sn-Pb alloys were electrodeposited from a commercial methanesulfonate electrolyte containing

0.34 mol/L Sn^{2+} . The electrolyte was prepared with high purity water with a resistivity of 18.3 M Ω cm. The cantilever samples were attached with plater's tape to a disk electrode assembly and rotated during plating at 100 rotations per min to provide reproducible hydrodynamic conditions. This rotation speed creates a uniform hydrodynamic boundary layer approximately 40 μm thick along the electrode surface [17]. All coupon surfaces except the cantilever were masked. Plating was performed at a constant current density of 60 mA/cm² in one liter of solution at 25 °C \pm 0.5 °C to various average thicknesses between 3 and 16 μm (determined by weight gain after plating). The anode was a 99.999 % pure Sn sheet. The plating efficiency was between (98 and 100) %. Thus hydrogen evolution is not thought to affect the results of this study. The coupons were removed from the bath while still electrified. At this current density, the plating rate is approximately 0.05 $\mu\text{m/s}$ and 320 s is required to form a 16 μm deposit. For the Sn-Cu deposits the Cu^{2+} concentration in the electrolyte was 15.0 mmol/L by the addition of copper methanesulfonate [$\text{Cu}(\text{CH}_3\text{SO}_3)_2$]. An examination of the alloy-electrolyte compositions reported in [12] indicates that the co-deposition of copper is diffusion-limited at this Cu^{2+} concentration and current density. For the Sn-Pb deposits the Pb^{2+} concentration in the electrolyte was 9.2 mmol/L by the addition of lead methanesulfonate [$\text{Pb}(\text{CH}_3\text{SO}_3)_2$].

After electrodeposition, the plating tape was dissolved with acetone and the samples were rinsed with deionized water. For each coupon, the position of the beam tip with respect to the frame was measured before plating, within 15 min after plating and then at various times up to 2×10^6 s (20 days). The height of the beam tip with respect to the frame was measured at three positions as shown in Fig.1. These measurements were done with the coupon horizontal in the two orientations with respect to gravity. Correction was made for the increased

thickness of the beam due to plating. The position of the beam at each time was taken as the mean of the six measurements. The change in position from the initial position (prior to plating) is defined as the deflection. A *negative* deflection means that the electrodeposit surface is *convex* indicating that the deposit wants to expand (positive stress-free strain), the constraint of the underlying substrate putting the deposit in biaxial in-plane compression.

The plated surfaces were examined without preparation for the presence of whiskers and/or hillocks using optical and scanning electron microscopy (SEM). Selected samples were prepared for optical and SEM metallographic cross-sectional examination by mounting in epoxy and using standard polishing procedures. Sn, Sn-Cu and Sn-Pb samples plated on amorphous carbon were prepared for chemical analysis and for transmission electron microscopy (TEM) by cold stage precision ion milling.

Tensile tests with strain gauges were conducted on the 150 μm thick phosphor bronze substrate material. Young's modulus and Poisson's ratio were determined to be 134 GPa \pm 1.6 GPa and 0.386 \pm 0.02 respectively. Microhardness measurements were performed on cross-sections of the 16 μm thick electrodeposits. A Knoop indenter with 1 gm load was employed and oriented with the long axis parallel to the plating surface. Using the approximation that the yield stress is 1/3 of the microhardness, yield strength values of 44 \pm 2 MPa, 64 \pm 4 MPa and 44 \pm 4 MPa were obtained for the pure Sn, Sn-Cu and Sn-Pb deposits respectively. The higher yield stress of the Cu-Sn deposits is likely due to the presence of the hard intermetallic particles. All measured stresses in the deposits are below these yield stress values.

4. Results

4.1 Surface Microstructure of Deposits

On pure Sn deposits, compact conical hillocks approx. 2 μm high by 2 μm wide appear within 900 s of plating. These appear to be grains that have risen from the surface. Within two days, approximately 10 % of the small hillocks grow while the others remain the same size. This process produces the bimodal surface structure shown in Fig. 2. Multiple EBSD patterns taken from the small and large conical hillocks show most to be single grains. Patterns taken from 26 conical hillocks surface showed no obvious preferred orientation. The single grain structure of the conical hillocks was confirmed by an SEM image of a FIB cross section (Fig. 3) on a 16 μm thick Sn sample [18]. We note a significant change in the as-plated columnar grain structure of the deposit under the hillock. Significant grain boundary motion has occurred in conjunction with the development of the hillock.

Filamentary whiskers and hillocks were evident on the Sn-Cu deposits within 2 days of plating. Fig. 4 shows SEM views of a 16 μm thick Sn-Cu alloy deposit surface. The hillocks are not conical and have a contorted appearance. They are also much larger (50 μm wide x 50 μm wide) than the conical hillocks in the pure Sn deposits. Whiskers appear to spew forth from approximately 10 % of these features. The whiskers appear first followed by continued accumulation of Sn at the base. The grain boundaries on the undisturbed part of the surface are difficult to identify because of a fine dispersion of particles and have been sketched in. These particles are Cu_6Sn_5 that have coarsened from the initially fine precipitates seen by TEM that formed within the Sn grains shortly after plating (as described below). To obtain a sense of the time scale during which the surface disturbances grow, Fig. 5 shows a sequence of SEM photographs of a feature that grew in volume with time. Because contorted hillocks and whisker filaments occur on the same sample (Fig. 4), Fig. 6 shows SEM images of FIB cross sections [18] at two positions on a single 16 μm thick Sn-Cu sample. Note that the as-

plated grains are columnar. The contorted hillock shape forms because of the activity of more than one grain under the disturbance and the IMC hindered grain boundary motion under the hillock. Grain boundary pinning appears to have been very effective under the filamentary whisker where no grain boundary motion has occurred in the deposit under the filament.

Fig. 7 shows SEM views of a 16 μm thick Sn-Pb electrodeposit surface. The surface is free of hillocks and whiskers at all times. Only grain boundary grooves are evident. The backscattered SEM image shows that coarsened Pb particles exist as separate grains mixed with Sn grains. A FIB cross section (Fig. 8) [18] shows that the grain structure of the Sn-Pb electrodeposit is *not* columnar. Compared to the Sn and Sn-Cu deposits, the Sn-Pb deposits have many more grain boundaries transverse to the growth direction. It is known that the co-deposition of Pb significantly reduces any crystallographic texture in the Sn by preventing columnar growth [19].

Examination of the surfaces of the various 3 μm and 7 μm thick deposits showed the same structures noted above. However after cantilever measurements were stopped, re-examination of the surfaces after 2.5 years showed that while the 7 and 16 μm thick deposits surfaces remained the same, the 3 μm thick Sn deposit had developed a very low density of conical hillocks and long filamentary whiskers and the 3 μm thick deposit of Sn-Pb had developed a low density of short 20 μm long whiskers. It is possible that excessive handling of the cantilevers led to these changes for the thin deposits.

4.2 Internal Deposit Microstructure, Composition and Microhardness

SEM micrographs of metallographic cross sections of the 16 μm (average) deposits of the three alloys are shown in Fig. 9. The columnar grain structure of the Sn and Sn-Cu deposits is confirmed. These samples were approximately one year old (3×10^7 s) when sectioned. In all three micrographs, a 1.5 μm to 2.5 μm thick scalloped intermetallic Cu_6Sn_5 layer is seen on the interface between the deposit and the substrate. A much thinner Cu_3Sn layer is also present but not visible. The thickness of the Cu_6Sn_5 layer is in general agreement with that described in the introduction. In the Sn-Cu deposits intermetallic Cu_6Sn_5 is also seen distributed throughout the deposit, primarily on Sn grain boundaries. Metallography of the Sn-Pb proved difficult, producing the large holes in the cross section. The intermetallic layer is visible but the deposit grain boundary structure and Pb phase location is not revealed.

Determining the deposit composition proved difficult due to the low solute levels, small sample volumes and the two-phase nature of the deposits. Several methods were used: inductively coupled plasma analysis (ICP), energy dispersive spectroscopy (EDS) in the SEM from area scans (10 μm in the plating direction by 20 μm) of cross sectioned 16 μm thick deposits, and the area fraction of Cu_6Sn_5 (excluding that on the bronze/Sn interface) for the Sn-Cu deposit. The area fraction of Pb in the Sn-Pb sample could not be measured due to polishing difficulties. The Cu concentration ranged between 1.4 % and 3.7 % mass fraction Cu depending on the method used. The Pb concentration ranged between 1.0 % and 3.5 % mass fraction Pb. Because the deposition conditions were tightly controlled, we do not believe this range represents true variation in sample composition. The expected Cu concentration, based on diffusion-limited Cu^{2+} and a diffusion coefficient of $5 \times 10^{-6} \text{ cm}^2/\text{s}$ [20], is 3.3 % mass fraction Cu. We will set the compositions to be 3 % mass fraction Cu and 2 % mass fraction Pb for the analysis below.

TEM examination (Fig. 10) of a Cu-containing deposit on glassy carbon one day after deposition shows fine intermetallic precipitates within the Sn grains and a few on the grain boundaries. It is well known that electrodeposition is capable of producing alloy deposits that are super-saturated; i.e., they contain more alloying addition than the phase diagram permits at the temperature of deposition [21]. It is likely that the fine IMC particles in Fig 10 form by precipitation from solution quite rapidly (within 10^3 s) and evidently coarsen over the period of one year when they appear mostly along the Sn grain boundary as seen in Fig 9. The rapid precipitation of IMC from supersaturated solid solution was confirmed using *in situ* synchrotron x-ray diffraction during and after the deposition of a Sn-Cu alloy onto a tungsten substrate [16]. This internal intermetallic precipitation was finished 30 min after plating. We note that supersaturation of Sn with up to 2.2 % mass fraction Cu has been reported by rapid solidification and immediate diffraction measurements at liquid nitrogen temperature [22].

TEM examination of a Pb-containing sample one day after deposition on glassy carbon showed extremely fine (10 nm) spherical precipitates of Pb. One month after plating, (Fig. 11), the Pb particles are approximately 50 nm tetragonally distorted cuboids within the grains and larger particles on the Sn grain boundaries. Table 1 summarizes the microstructure.

Table 1 - Summary of microstructure observations for 16 μm thick deposits

	Sn	Sn-Cu	Sn-Pb
Surface defects	Conical hillocks	Contorted hillocks and filamentary whiskers	None
Sn grain structure	Columnar, mobile	Columnar, immobile	Equiaxed
Initial alloy structure	-	Fine Cu_6Sn_5	Fine Pb
Aged alloy structure	-	Coarse Cu_6Sn_5 on grain boundaries	Sparse equi-axed Pb grains

Cu_6Sn_5 forms slowly on the deposit / substrate boundary for all.

4.3 Hillock Volume

Measuring the total amount of material pushed up above the deposit surface during whisker growth is difficult due to the irregularity of the shapes. The regularity of the conical hillocks observed on the 16 μm thick pure Sn electrodeposits provides an opportunity for such a measurement. The distribution of projected areas (onto the plated surface) of the hillock population was measured by quantitative metallography 7.86 $\times 10^6$ s after plating. Each hillock was assumed to be a cone with a radius derived from its measured projected area and with an apex semi-angle (estimated from FIB cross sections) of 45° for the small hillocks and 58° for the large hillocks of the bimodal distribution. The total hillock volume per unit plated surface area is 0.012 μm . We estimate that about a third of this volume develops within 1 hour of plating. Dividing by the deposit thickness, 16 μm , an average volumetric plastic strain, $\Delta V/V$, of 8×10^{-4} was determined. An estimate of the in-plane biaxial stress that was relieved by this hillock formation [23] is

$$\Delta\sigma = \frac{E_f'}{2} \frac{\Delta V}{V} \quad [3]$$

where E_f' is the biaxial modulus of Sn (78 GPa, see Table 2). The compressive stress reduction is 30 MPa. This number is of the same order as, but about twice, the stress relaxation measured over the 7.86 $\times 10^6$ s by the cantilever beam measurements.

4.4 Cantilever beam deflection measurements

4.4.1 Initial Deflection – Plating Stress

After release from the rotating assembly, the deposit side of all cantilever beams was immediately convex; i.e. the deflection is negative. This indicates that the deposit wants to expand with respect to the beam and is thus in a state of compressive stress. Over a period of several weeks, the cantilevers become less convex; i.e., the deflection becomes less negative.

The deflection vs. time measurements are given in Fig. 12. Remarkably, some samples develop positive displacement with time. The data are fit with a power law in time, which is used for the data reduction described below.

First we examine the average stress in the deposit determined from the earliest deflection measurement at approximately 10^3 s. As described above, the intermetallic on the bronze/Sn interface is quite thin (20 nm) at this time and can be neglected. Because of the 16 μm thick electrodeposit, we will employ the first order correction to Stoney's equation. If the bi-axial in-plane stress in the deposit before it is released from the rotating disk is assumed to be uniform, the stress to first order depends on the moduli. However the average stress in the deposit after it is released, σ_f , does not depend on the moduli and is given by

$$\sigma_f = \frac{E'_s}{6} \frac{d_s^2}{d_f} K \left[1 - \frac{d_f}{d_s} \right] = \frac{E'_s}{3} \frac{d_s^2}{d_f} \frac{\delta}{L^2} \left[1 - \frac{d_f}{d_s} \right] \quad [4]$$

where the notation is defined in Table 2. See reference [24] for a discussion of various approximations for thick deposits.

Table 2: Parameters for Stoney's Equation and other mechanical parameters

E'_s = Substrate biaxial modulus = $E_s/(1-\nu_s)$ = 216 GPa, (E_s =134 GPa, ν_s =0.386)
d_s = Substrate thickness = 152 μm
d_f = Film thickness = 3 μm , 7 μm , 16 μm
L = Beam Length = 20 mm
δ = Deflection of beam from position prior to plating
K = Curvature of beam = $2\delta/L^2$
E'_f = Sn biaxial Modulus = 78 GPa, (E_s =50GPa, ν_s =0.357 [25])
E'_{IMC} = Cu ₆ Sn ₅ biaxial Modulus = 122 GPa, (E_s =86 GPa, ν_s =0.3 [26])

Fig. 13 shows a plot of the initial compressive stress (approx. 15 min after plating) versus deposit thickness for the three deposit compositions using the parameter values in Table 2.

All stresses are compressive. For each alloy, the initial stress becomes more compressive with

increasing thickness. Because the diffusion fields in the electrolyte, and thereby the deposit alloy compositions, reach steady state within the first 0.1 μm of deposition due to the rotation of the electrode, the observed stress-thickness relationship cannot be attributed to a concentration gradient in the deposition direction. The reason for the increase in the magnitude of the compressive stress with deposit thickness is unclear.

Regardless of deposit thickness, the Sn-Cu deposits have the highest compressive stress, the pure Sn has intermediate compressive stress, and the Sn-Pb deposit has the lowest compressive stress. A positive correlation exists between the magnitude of the compressive stress and the degree of disruption of the surface morphology; viz., the Sn-Cu samples have whiskers and large contorted hillocks, the pure Sn has only small hillocks and the Sn-Pb alloys are free of hillocks and whiskers.

4.4.2 Deflection vs. Time

The measured deflection histories are shown in Fig. 12. The beams return toward their initial positions with many of the samples actually passing through the initial position. A simple Stoney analysis would imply that the deposit stress begins compressive and becomes tensile with time. However this is not necessarily correct as several processes are taking place.

Among them are: a) intermetallic formation on the bronze/Sn interface, b) uniform creep of the electrodeposit, and c) for some samples, hillock and whisker formation. To determine the stress and the strain rate in the Sn and Sn alloy deposits from the deflection data, we need to perform a “two layer Stoney analysis,” one layer for the deposit and one for the growing IMC. The details of a model are given in the Appendix and an analysis of the time dependence will be deferred to the discussion.

5 Discussion

5.1 Molar volume of Sn-Cu and Sn-Pb alloys

Before we can analyze the reasons for the various states of stress in the deposit, it is useful to consider the molar volume (volume per mole of atoms) for Sn-Cu and Sn-Pb alloys as summarized by Figs. 14. For Sn-Cu, crystallographic data was used for the pure elements and the Cu-rich phases. For Cu_6Sn_5 , Fields et al. [26] measured a density of 8.28 g/cm^3 that converts to $10.6 \text{ cm}^3/\text{mol}^1$ (of atoms) using the composition of 0.44 atomic fraction Sn given by [27]. In the same manner, the density of Cu_3Sn , 8.90 g/cm^3 , converts to $8.6 \text{ cm}^3/\text{mole}$. The equilibrium solubility of Cu in solid Sn is very small: 6×10^{-3} mass fraction Cu at $227 \text{ }^\circ\text{C}$ [28] and 10^{-7} mass fraction Cu at room temperature (thermodynamic calculation [29]). As noted above, however there is evidence from Fig. 10 and [16] that a supersaturated solid solution of Cu in Sn is formed by the electrodeposition process. Hence, we require an estimate of the molar volume of Sn supersaturated with Cu, $\text{Sn}(\text{Cu})$. Given the work on fast diffusion² of Cu in Sn and the presumption that the Cu is dissolved interstitially in Sn [30, 31] and in addition assuming that the partial molar volume of interstitial Cu is zero, the volume per mole of atoms of supersaturated $\text{Sn}(\text{Cu})$ is shown in Fig. 14 and is given by

$$V_M^{\text{Sn}(\text{Cu})} = 16.28(1 - X_{\text{Cu}}) \quad [5]$$

where X_{Cu} is the mole fraction of Cu. These considerations would imply that the lattice parameter of Sn is unchanged by the interstitial Cu, a result consistent with [16]. The lattice parameters for the Sn-Pb system are summarized by [32]. Specifically, Sn rich $\text{Sn}(\text{Pb})$ solid solution up to 0.012 mass fraction Pb were measured at $183 \text{ }^\circ\text{C}$ by [33]. After conversion from kX units to SI units and changing the value of the intercept to get the accepted value for pure Sn at room temperature, the results are

¹ The measured density agrees with the measured lattice parameters of the B8_2 ($\text{P6}_3/\text{mmc}$) structure of Cu_6Sn_5 if one considers the vacant 2d Wyckoff sites required to achieve the correct phase composition.

$$V_M^{Sn(Pb)} = 16.28 + 3.52X_{Pb} \quad [6]$$

where X_{Pb} is the mole fraction of Pb. Extrapolation of this expression beyond the equilibrium solubility is plotted in Fig. 14.

We extract a few numbers from Fig. 14 for use below. First, the formation of a layer of Cu_6Sn_5 at an interface between Sn and Cu is considered. The volumetric strain for this process can be read directly from the graph or determined analytically. It is the difference between the molar volume of the Cu_6Sn_5 and the molar volume of an unalloyed mixture of pure Cu and pure Sn of the same average composition as the intermetallic. The fractional change is -0.056. In other words, the IMC takes up 5.6% less volume than a rule of mixture combination of the Sn and Cu reactants from which the IMC forms.

From Fig. 14 we can also extract the volume change when precipitation of Cu_6Sn_5 occurs from a supersaturated Sn(Cu) solid solution of mass fraction 3 % Cu. It is the difference between the molar volume of the supersaturated solution and the volume of a equilibrium mixture of Sn and Cu_6Sn_5 of the same average composition as the supersaturated solution. For a deposit of 3 % mass fraction Cu (5.5 % atom fraction), the fractional change in volume is +0.022. That is, the volume of a supersaturated solution of Sn(Cu) expands by 2.2 % when it transforms to an equilibrium mixture of Sn and Cu_6Sn_5 phases. Finally, the volume change of material that undergoes precipitation of Pb from a supersaturated Sn(Pb) solution can be obtained from the graph. For a deposit of 2 % mass fraction Pb (1.16 % atom fraction), the

² We note that Ni also exhibits fast diffusion in Sn [34] due to its interstitial nature and would be expected to exhibit the same molar volume behavior.

fractional change in volume is -0.0013. That is, the volume of a supersaturated solution of Sn(Pb) shrinks by 0.13 % when it transforms to an equilibrium mixture of Sn and Pb phases.

5.2 Initial Plating Stress

Understanding the causes of growth stress in thin films formed by electrodeposition (and by other methods such as condensation from the vapor [35]) are active areas of research. We consider here only the difference between the stress in the pure Sn, and those in the alloy deposits. We assume that deposits of the same thickness are formed with the same growth stress as pure Sn and that the precipitation process in the alloy shortly after deposition attempts to alter the volume and hence change the stress prior to the first measurement. Table 3 gives the experimentally determined deviation of the stress-free strain values above or below that determined for the pure Sn. Also given is 1/3 of the change in the deposit volumetric strain expected from the change in molar volumes for precipitation from supersaturated solid solutions described in Section 5.1.

Table 3: Effect of Alloying Addition on Initial Stress of 16 μm deposits

Alloy	Measured initial stress (MPa)	Corresponding stress-free strain	Deviation of stress-free strain from that for pure Sn	1/3 of volume change due to ppt. of Cu_6Sn_5 or Pb from Cu or Pb supersaturated Sn
Sn	-15.5	2.3×10^{-4}	---	---
Sn-2%Pb	-4.0	0.6×10^{-4}	-1.7×10^{-4}	-4×10^{-4}
Sn-3%Cu	-36.5	5.6×10^{-4}	3.3×10^{-4}	7×10^{-3}

Note from the Appendix that $\varepsilon_f^0 = \varepsilon_f^T - \frac{\sigma_f}{E_f} = -\frac{4}{3} \frac{\delta}{L^2} d_s - \frac{\sigma_f}{E_f}$

If the model worked perfectly, the numbers in each row of the last two columns should be the same. Similar results are obtained for the 3 μm and 7 μm thick electrodeposits, except the

experimental increments get smaller as the thickness decreases. In conclusion, this model produces the correct trends for the alloys if not the correct numerical values; viz., that the addition of Cu increases that state of compression over pure Sn and that Pb causes the stress to become less compressive. The quantitative errors may be due to the difficulties in measuring the deposit concentrations and/or the assumption that interstitial Cu has zero partial molar volume. A non-zero value would decrease the proposed amount of expansion due to Cu_6Sn_5 precipitation listed in the last column of Table 3.

5.3 Time dependence of beam deflection

The use of the model and equations in the Appendix requires a value for the stress in the IMC layer, σ_{IMC} (more properly the stress free strain, ε_{IMC}^0). An upper bound for the intermetallic stress free strain is obtained using 1/3 the value of the volumetric strain for planar IMC formation from pure Sn and Cu; viz., $\varepsilon_{IMC}^0 = -0.02$ (see section 5.1). Using the modulus for IMC in Table 2, $\sigma_{IMC} \approx +4.8$ GPa. This value is an upper bound because the IMC may not swell isotropically; e.g., it might expand more in the growth direction to reduce the strain energy. A second estimate is obtained experimentally [16] from *in situ* wafer curvature measurements after the deposition of 100 nm of Sn onto a Cu coated glass cantilever. After 20 nm of IMC has formed, a beam deflection consistent with a tensile stress in the IMC of +1.2 GPa was obtained. A more appropriate estimate for thicker IMC layers comes from the following experiments. For three pure Sn cantilever electrodeposits, 16 μm thick and aged for approximately 3×10^7 s, the Sn was removed by dissolution in concentrated HCl. This procedure leaves the approximately 2.5 μm thick IMC behind. The deflections of the beams (compared to the original unplated position) were +7 μm , +30 μm and +37 μm ; i.e., toward

the deposit side. From these experiments we conclude that σ_{IMC} is between 11 MPa and 62 MPa tension. ($\varepsilon_{IMC}^0 = -10^{-4}$ and -5.1×10^{-4}). Lee and Lee [11] performed similar stripping experiments but unfortunately did not report the IMC stress. Due to the uncertainty in the proper value of ε_{IMC}^0 , we will compute the stress in the electrodeposit using the deflection data for several assumed values of ε_{IMC}^0 .

Using the measured deflections and the model and equations in the Appendix, we plot in Fig. 15 the deposit stress, σ_f , for a 7 μm thick pure Sn deposit for several values of ε_{IMC}^0 . With $\varepsilon_{IMC}^0 = 0$, the deposit stress changes sign from compression to tension at the same time that the beam deflection changes sign; the deflection is proportional to $\sigma_f d_f + \sigma_{IMC} d_{IMC}$, (Eqns. A1 & A3). For a value $-\varepsilon_{IMC}^0 > 2.5 \times 10^{-3}$, the stress remains compressive for all time. This confirms the idea presented by several authors that IMC formation compresses the Sn, but slowly.

The total deposit strain is proportional to the deflection (Eqns. A1 & A4) and is positive if the deflection is negative. We assume that deposit stress free strain, ε_f^0 , is positive and constant at times greater than 10^3 s and is due to the plating plus the fast precipitation processes for the alloys. (Values for the 16 μm samples are reported in Table 3.) The relative sizes of the elastic and plastic parts, ε_f^E and ε_f^P , depend on the assumed value of ε_{IMC}^0 . Fig. 16 shows the total deposit strain, ε_f^T vs. time and its parts for two different values of ε_{IMC}^0 . The elastic strain is proportional to the stress. After subtracting this from the total strain, one obtains the sum of the stress free and plastic strain. The plastic strain rate history is determined by differentiation. Fig. 17 shows examples of plots of deposit plastic strain rate vs. deposit stress.

One slides down the creep curve as time progresses. Such plots constitute the experimentally obtained average compression creep response of the deposits if we can assume that steady state creep behavior applies at each instant. Reassuringly, use of a positive value of ε_{IMC}^0 (all measurements yield negative values) leads to unrealistic plastic response; the sign of the stress and strain rate are not the same. Extremely negative values of ε_{IMC}^0 lead to equally unphysical creep curves where the stress exponent increases with decreasing compressive stress. These considerations place bounds on the value of ε_{IMC}^0 .

The result for the deposit stress and deposit plastic strain rate for the 16 μm thick deposits are shown in Fig. 17 plotted as $\log(-\text{strain rate})$ vs. $\log(-\text{stress})$ for three values of ε_{IMC}^0 , 0, -0.001, -0.002 that span the full range of reasonable values. For large compressive stress (early times), the curves are independent of ε_{IMC}^0 and exhibit stress exponents of approximately 3, 6, and 15 for the Sn-Pb, Sn and Sn-Cu respectively. We also note that Sn-Pb creeps faster than pure Sn, which in turn creeps faster than Sn-Cu. For smaller values of compressive stress (later times), the creep curves show considerable dependence on ε_{IMC}^0 . The most negative value of ε_{IMC}^0 cause stress exponents that increase as stress decreases, a situation considered unphysical (see for example the Sn and Sn-Cu sample). The best that can be concluded is that the stress in the intermetallic lies between zero and 300 MPa (tension) and helps maintain the compressive stress in the deposit over longer periods of time. However, this analysis suggests that IMC formation on the Cu/Sn interface does not greatly increase the compressive stress over the level due to the initial plating stress.

5.4 Creep as a mechanism for whisker / hillock formation.

Fig. 17 shows the in-plane components of stress and plastic strain rate. If the in-plane creep is uniform, the electrodeposit would swell slightly and uniformly in thickness as the compressive stress relaxes. Indeed for incompressible plasticity, the plastic strain (strain rate) normal to the electrodeposit surface equals minus two times the in-plane strain (strain rate).

We consider here that hillock and whisker formation are forms of creep that are not uniform whose average amount is given by the measurements. We presume then that the creep curve for Sn-Pb shown in Fig. 17 represents uniform creep alone because no whiskers, cones or hillocks form; whereas the creep curves for Sn and Sn-Cu also include the nonuniform creep that produces the surface disruption. In other words the hillock and whisker formation is part (or all) of the compression creep response of these materials when constrained by a substrate. We note that the creep rates of the pure Sn and Sn-Pb deposits are much slower than those reported for bulk samples of similar materials with similar grain structures [36, 37].

As mentioned in the introduction, diffusional creep has been employed to explain hillock growth in thin films. Following this approach, Tu [10] and Hutchinson [38] have proposed models for whisker growth velocity based on an imposed constant in-plane compressive stress and grain boundary diffusion of Sn to the whisker base. With whiskers a distance $2b$ apart and with diameter $2a$, both models arrive at a tip growth velocity v given by

$$v = -\ell \left[\frac{2D_{gb}\Omega}{RTa^2 \ln(b/a)} \right] \sigma_f \quad [7]$$

where Ω is the molar volume of Sn, D_{gb} a grain boundary diffusion coefficient, RT is the Boltzmann factor and a signed stress, σ_f , has been used. A stress gradient in the deposit with cylindrical symmetry under each whisker is assumed to drive the flux of Sn toward that

whisker. The length differs in the two models significantly depending on the geometrical details. The model of Hutchinson et al., which uses $\ell = d_f$ and replaces D_{gb} with $D_{gb} \frac{2\lambda}{g}$ where λ and g are the effective thickness of a grain boundary and the grain size respectively, leads to the correct order of magnitude of whisker growth rate using literature accepted values of the grain boundary diffusion coefficient for Sn [39]. From these models, one can compute the plastic strain rate normal to the deposit averaged over the entire deposit surface as $\nu a^2 / b^2 d_f$; giving an in-plane creep rate for an incompressible deposit of $-\nu a^2 / 2b^2 d_f$ or

$$\dot{\epsilon}_f = \frac{\ell}{d_f} \frac{\Omega D_{gb}}{RTb^2 \ln\left(\frac{b}{a}\right)} \sigma \quad [8]$$

We note that this prediction is linear in stress and would produce a creep rate with slope of unity as superimposed in Fig. 17, where we have used $\ell = d_f$, $\lambda D_{gb} = 6 \times 10^{-22} \text{ m}^3/\text{s}$ [39], $g = 3 \text{ } \mu\text{m}$, $\Omega = 1.7 \times 10^{-5} \text{ m}^3/\text{mol}$, $a = 2 \text{ } \mu\text{m}$ and $b = 100 \text{ } \mu\text{m}$.

It is interesting to note, despite the approximations of this whisker growth model, that the derived average strain rate is roughly tangent to the creep curves for the pure Sn, lies below the creep curves for Sn-Pb and cuts through the creep curve for Sn-Cu. As a mechanism of creep, whisker growth would then be least active for Sn-Pb, be marginal for pure Sn and occur readily for Sn-Cu. For Sn-Cu, creep likely occurs by a mechanism with high exponent before whisker creep becomes dominant at lower compressive stress. This may be related to the observation that whisker formation appears to have an ‘‘incubation time.’’

The above models for whisker growth need improvement. A detailed model is beyond the scope of the present paper, but it would be a special case of Coble creep [40]. The diffusion potential (chemical potential of Sn atoms minus chemical potential of vacancies) is highest for grain faces with the most compressive normal stress. This would correspond to grain faces with normals lying in the plane of the deposit due to the bi-axial in-plane stress state. Oblique grain faces would have lower diffusion potential and grain faces parallel to the deposit surface would be least. (The surface of the deposit would also have the least diffusion potential, but we presume surface diffusion is suppressed by native oxide.) This difference in diffusion potential causes a flux of Sn along the normal grain faces to oblique faces. If many oblique or parallel faces are located within the deposit (as with the Sn-Pb deposits), creep is relatively uniform and no hillocks/whiskers would occur. Averaged over many grains this process leads to a slight thickening of the deposit and a reduction in the in-plane stress. If oblique or parallel faces occur rarely, as in a columnar structure typical of Sn and Sn-Cu, the diffusion flux is forced toward the free surface. Any oblique grain face near, but under, the deposit surface would be ripe for accumulation of Sn and pushing of the grain upward to produce surface features. As with any diffusional creep process, grain boundary sliding and accommodation must occur simultaneously [41]. A proper model must assess the path through a three dimensional network of grain faces with normals lying in the plane of the deposit connecting to oblique grain faces near the deposit surface, for example at a small grain as shown the cross sectional schematic in Fig. 18. Only a few spurious grains formed in the deposit at the end of deposition permit this process.

Fig. 19 shows different situations depending on the mobility of the grain boundaries of the columnar structure. Fig 19a shows the case for pure Sn deposits, where the hillock grain can

broaden laterally by grain boundary migration; it never forms a filamentary whisker. For very thin deposits, hillock base broadening may be halted when the hillock grain bottom has impinged on the layer IMC. If sufficient compressive stress remains, the hillock may then grow in a more whisker-like manner. Such a process may be important for deposits with thickness the same as the lateral grain size. In a film under stress, the seeds of a model for this lateral grain boundary motion and surface upheaval on the trailing side can be found in [42]. Many hillocks appear to have a small flat top at their center indicating the original location of the hillock grain prior to the migration of its boundaries. In Fig. 19b is depicted the situation for the Sn-Cu deposits; the grain boundaries are pinned by the internal IMC particles formed by precipitation from supersaturated solution. Hillock grain base broadening is hindered and the upward motion of material is concentrated into contorted hillocks or whiskers. Contorted hillocks occur when several surface grains with oblique internal faces in close proximity are present; hence the multi-grained nature seen in Fig. 6. Whiskers occur when a single surface grain with immobile oblique internal faces persists in time for the Sn flux to continually accrete.

6. Conclusions

1) Plating on cantilever beam samples, shows that compressive stresses are present in high purity bright Sn electrodeposits within 15 minutes after plating. Intermetallic growth along the Sn/Cu interface should be insignificant (6 nm thickness) over this short time at room temperature. Thus compressive stresses are intrinsic to the plating process under the conditions of our experiments.

2) Co-deposition of Sn with Cu or Sn with Pb in the amount of a few mass percent alters the compressive stress compared to pure Sn by the time of first measurement. Larger compressive stress is generated in the electrodeposit with Cu addition to the electrolyte;

smaller compressive stress is generated in the deposit by a Pb addition to the electrolyte. The increase/decrease in compressive stress for the alloys is due to volume changes of the deposit caused by the solid state precipitation of Cu_6Sn_5 / Pb particles by metallurgical precipitation from the supersaturated Sn-Cu / Sn-Pb solid solution formed by the plating process.

3) Cu addition does not alter the columnar grain structure found in pure Sn deposits, whereas the Pb addition causes an equi-axed grain structure to develop.

4) The analysis of the time dependence of the measured beam deflections indicates that the additional compressive stress due to intermetallic formation on the deposit / beam interface over long time periods is of the same order of magnitude as the plating stress.

5) Whiskers and contorted hillocks are observed on the Sn-Cu deposit surfaces, conical hillocks are observed on the pure Sn deposits and no surface disturbances are found on the Sn-Pb deposits.

6) We propose that the compressive stress in the deposits relaxes by Coble creep (grain boundary transport of Sn and vacancies). For the equiaxed structure of the Sn-Pb deposits, transport between interior grain faces with different normal stress permits uniform swelling of the deposit thickness and no localized surface disturbance. For the columnar structures of the Sn and Sn-Cu deposits, the Sn flows toward the free surface. In the absence of surface transport due to native oxide, the Sn accumulation is localized to oblique grain faces near but under the free surface that forces the grain upward.

7) The lack of lateral grain boundary mobility of the columnar structure in the Sn-Cu deposits caused by precipitate pinning is thought to promote whisker formation by maintaining a laterally small grain where Sn flux accumulates. Rather benign (electronically) hillock formation occurs in pure Sn due to extensive lateral grain boundary migration.

8) A whisker mitigation strategy based on this work is to avoid impurities in the electrolyte such as Cu that are fast diffusers and hence occupy interstitial sites in the Sn lattice.

Electrolytes containing solutes occupying substitutional sites in the Sn lattice and whose precipitation tends to reduce the volume of the deposit such as Pb should be beneficial.

Additives that break up the columnar structure and promote the formation grain boundaries parallel to the deposit surface, would allow uniform creep of electrodeposits without the necessity of diffusion of Sn to the proximity of the free surface where surface upheaval (whiskers) can occur.

Acknowledgements

The authors are indebted to R. Parke and S. Claggett for the TEM sample preparation, to R. Fields for the phosphor bronze mechanical measurements, U. R. Kattner for thermodynamic calculations and to Daniel Josell for many fruitful discussions. Thanks are also in order to G. Galyon and M. Palmer for the FIB pictures, which greatly clarified the microstructures.

Appendix: Two layer time dependent beam deflection

We develop a model to describe the time dependent deflection of the beam caused by two sources: 1) an initial residual stress in the deposit, and its relaxation due to creep and 2) a layer of IMC that forms between the Sn and Cu substrate which has a different volume than the Sn and Cu from which it formed. This is performed to clarify the stresses in each layer, which can not be individually determined from the beam deflection. For this model, we will employ the thin deposit approximation, $\frac{d_f}{d_s} \ll 1$ to avoid unnecessary complication.

Let σ_i , d_i , ε_i E_i be the stress, thickness, strain and modulus in layer i where $i = IMC$ or f for the planar IMC layer and electrodeposited film respectively. Let the beam curvature be given by

$$K(t) = \frac{1}{r(t)} = \frac{2\delta(t)}{L^2} \quad [A1]$$

where $\delta(t) > 0$ if the electrodeposit surface is concave (deposit on top, curved up). To treat the fact that the IMC layer thickens with time and the Sn layer thins with time, we use

$$\begin{aligned}
d_{IMC}(t) &= \sqrt{Bt} \\
d_f &= d_f^0 - s d_{IMC}(t) \\
d_s &= d_s^0 - (1-s)d_{IMC}
\end{aligned}
\tag{A2}$$

where $s \approx 5/11$. With these expressions, the reduction of the Sn deposit thickness and the beam thickness due to IMC formation is included. For $d_{IMC}, d_f \ll d_s$, balance of moments and forces for the substrate and the two layers yields

$$\sigma_{IMC}(t)d_{IMC}(t) + \sigma_f(t)d_f(t) = \frac{E_s'}{6}(d_s(t))^2 K(t).
\tag{A3}$$

With the thin approximation, the total strain in both layers (measured from a flat beam) is the same and is given by

$$\varepsilon_{IMC}^T = \varepsilon_f^T = -\frac{2}{3}d_s(t)K(t)
\tag{A4}$$

The total strain in the IMC layer will be assumed to be the sum the stress-free strain due to its volume change from the reactants and its stress dependent elastic strain

$$\varepsilon_{IMC}^T = \varepsilon_{IMC}^0 + \varepsilon_{IMC}^{el}
\tag{A5}$$

with

$$\sigma_{IMC} = E_{IMC}' \varepsilon_{IMC}^{el} = E_{IMC}' [\varepsilon_{IMC}^T - \varepsilon_{IMC}^0].
\tag{A6}$$

The total strain in the Sn deposit will be assumed to be the sum of the stress free strain due to the electrodeposition process (plus the fast precipitation processes in the alloys), stress dependent elastic and plastic strains

$$\varepsilon_f^T = \varepsilon_f^0 + \varepsilon_f^{el} + \varepsilon_f^{pl}
\tag{A7}$$

with

$$\sigma_f = E_f' \varepsilon_f^{el} = E_f' [\varepsilon_f^T - \varepsilon_f^0 - \varepsilon_f^{plastic}]
\tag{A8}$$

and

$$\dot{\varepsilon}_f^{pl} = f(\sigma_f)
\tag{A9}$$

where the dot denotes a time derivative. The function $f(\sigma_f)$ could represent power law creep for example of the form

$$\dot{\varepsilon}_f^{pl} = K \sigma_f^n.
\tag{A10}$$

For choices of a parabolic growth constant B , and a value for ε_{IMC}^0 , plus Eqns. 1 & 4, one can extract $\sigma_f(t)$ and the quantity $[\varepsilon_f^0 + \varepsilon_f^{plastic}(t)]$ or its time derivative $\dot{\varepsilon}_f^{plastic}(t)$ from the measured data, $\delta(t)$. One can then plot log strain rate vs. log stress for the electrodeposit to estimate the function, Eqn. [A8]. Because the stress and strain rates are negative (compression creep), absolute values are used for such a plot.

Alternately, one can convert these equations to a system of coupled ordinary differential equations for $\delta(t)$, $\sigma_f(t)$, $\sigma_{IMC}(t)$ and $\varepsilon_f^{plastic}(t)$ for a given creep law and the other materials parameters. Numerical solution shows how the electrodeposit stress is affected by the growing

IMC. In general the stress in the film becomes slightly more compressive due to the IMC growth. The amount is sensitive to the how positive is the chosen value of ε_{IMC}^0 .

References

1. Furuta N, Hamamura K. Jap. J. Appl. Phys 1969; 8 :1404.
2. Kabakian L, Chason E, Kumar KS, Spring MRS 2003.
3. Fisher RM, Darken LS, Carroll KG. Acta Met 1954; 2: 368.
4. Arnold SM. Plating, 1966; 53: 96.
5. Gaylon GT, "Annotated Tin Whisker Bibliography," National Electronics Manufacturing Initiative Inc. (NEMI), Herdon VA, July 2003. (www.nemi.org)
6. Chadhari P. J. Appl. Phys 1974; 45: 4339.
7. Jackson MS, Li C-Y. Acta Met 1982; 30: 1993.
8. Doerner MF, Nix WD. CRC Critical Reviews in Solid State and Materials Sciences 1988; 14: 225.
9. Tu KN. Acta Met 1973; 21: 347.
10. Tu KN. Phys. Review B-Condensed Matter 1994; 49: 2030.
11. Lee BZ, Lee DN. Acta Mat 1998; 46: 3701.
12. Moon K-W, Williams ME, Johnson CE, Stafford GR, Handwerker CA, Boettinger WJ, in "Proceedings of the Fourth Pacific Rim International Conference on Advanced Materials and Processing," The Japanese Institute of Metals, Sendai, Japan, 2001, Hanada S, Zhong Z, Nam SW, Wright RN, eds., pp. 1115-1118.
13. Weil R. Plating 1971; 58: 137.
14. Onishi M, Fujibuchi H. Trans. J. Inst. Metals 1975; 16: 539.
15. Tu KN, Thompson RD. Acta Met 1982; 30: 947.
16. Stafford GL, Bertocci U, Guyer JE, NIST (2004) unpublished research.
17. Bard AJ, Faulkner LR. "Electrochemical Methods: Fundamentals and Applications," (New York: John Wiley and Sons, Ltd., 1980) pp. 288.
18. Galyon GT, Palmer M, IBM, 2004, unpublished research.
19. Petersson I, Ahlberg E. J. Electroanal. Chem. 2000; 485: 166.
20. Tindall GW, Bruckenstein S. Anal. Chem., 1968; 40: 1402.
21. Brenner A., "Electrodeposition of Alloys". Vol. 1. 1963, New York: Academic Press. p.195.
22. Kane RH, Giessen BC, Grant NJ. Acta Met 1966; 14: 605.
23. Kim D-K, Nix WD, Deal MD, and Plummer JD. J. Mater. Res 2000; 15 :1709
24. Brenner A, Senderoff S. J. of Research of the NBS 1949; 42: 105
25. Metal Reference Book, Smithells CJ, 4th edition, Plenum Press, NY 1967.
26. Fields RJ, Low III SR, , Lucey, Jr. GK. in "Metal Science of Joining," Cieslak MJ, Perepezko JH, Kang S, Glicksman, ME, eds., The Minerals, Metals & Materials Society, Warrendale, PA., pp. 165-173, 1992.
27. Saunders N, Miodownik AP. Bull. of Alloy Phase Diagrams 1990; 11: 278
28. Homer CE, Plummer H. J. Inst. Metals 1939; 64:169.
29. Kattner UR, NIST , Gaithersburg, MD, 2002, unpublished research.
30. Dyson BF, Anthony TR, Turnbull D. J. Appl. Physics 1967; 38: 3408.
31. Warburton WK, Turnbull D. Thin Solid Films 1975; 25: 71
32. Karakaya I, Thompson WT. Bull. of Alloy Phase Diagrams 1988; 9: 144.
33. Lee JA, Raynor GV. Proc. Phys. Soc. 1954; 67: 737.

34. Yeh DC, Huntington HB. Phys. Rev. Lett 1984; 53: 1469.
35. Floro JA, Chason E, Cammarata RC, Srolovitz D, MRS Bulletin 2002; 27:19.
36. Schneibel JH, Hazeldine PM. J. Matl. Sci 1983; 18: 562.
37. McCabe RJ and Fine ME, Metall.& Mater. Trans. 2002: 33A:1531.
38. Hutchinson B, Oliver J, Nylén M, Hagström J, Mat. Sci. For 2004; 467-470: 465.
39. Kaur I, Gust W. "Handbook of Grain Boundary and Interface Boundary Diffusion Data", (Ziegler Press, Stuttgart 1989 Vol. 2, p. 1277.
40. Coble RL. J. Appl. Phys. 1963; 34: 1679.
41. Raj R, Ashby MF. Met. Trans. 1971; 2: 1113.
42. Genin FY, J. Appl. Phys. 1995; 77: 5130.

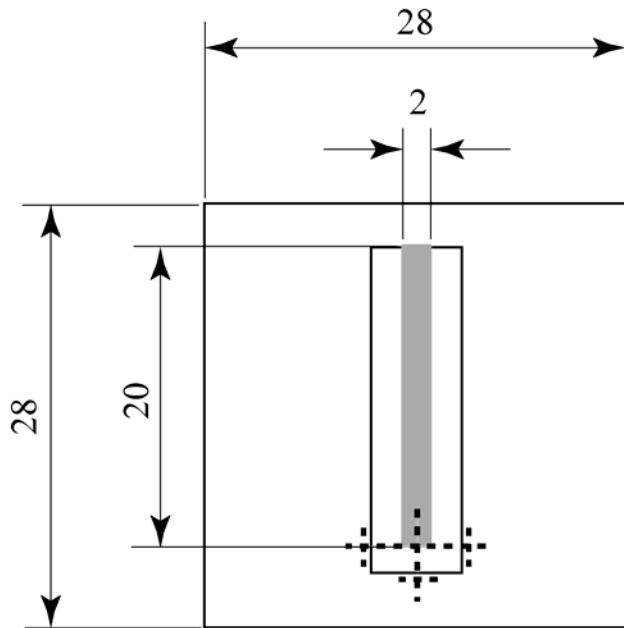


Fig. 1: Drawing of a cantilever beam coupon with plated region shown in gray. The three frame positions used for tip position measurement are indicated. Dimensions in mm.

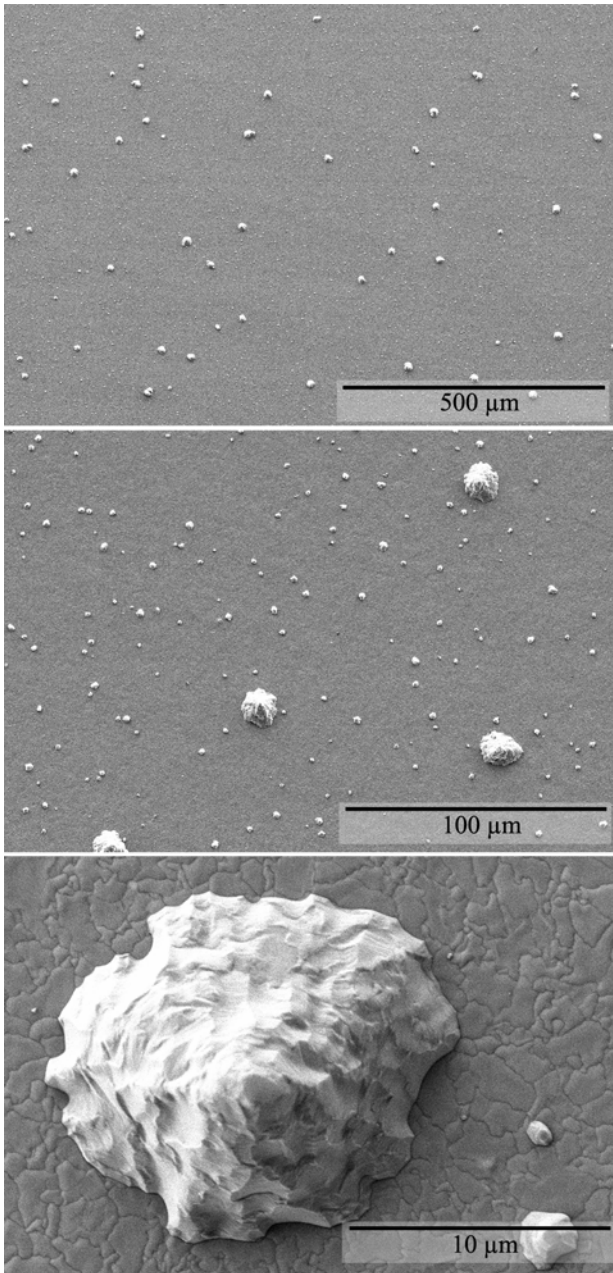


Fig. 2: Low, intermediate and high magnification SEM micrographs of the electrodeposit surface of a 16 μm thick pure Sn electrodeposit on a cantilever beam showing bimodal size distribution of conical hillocks.

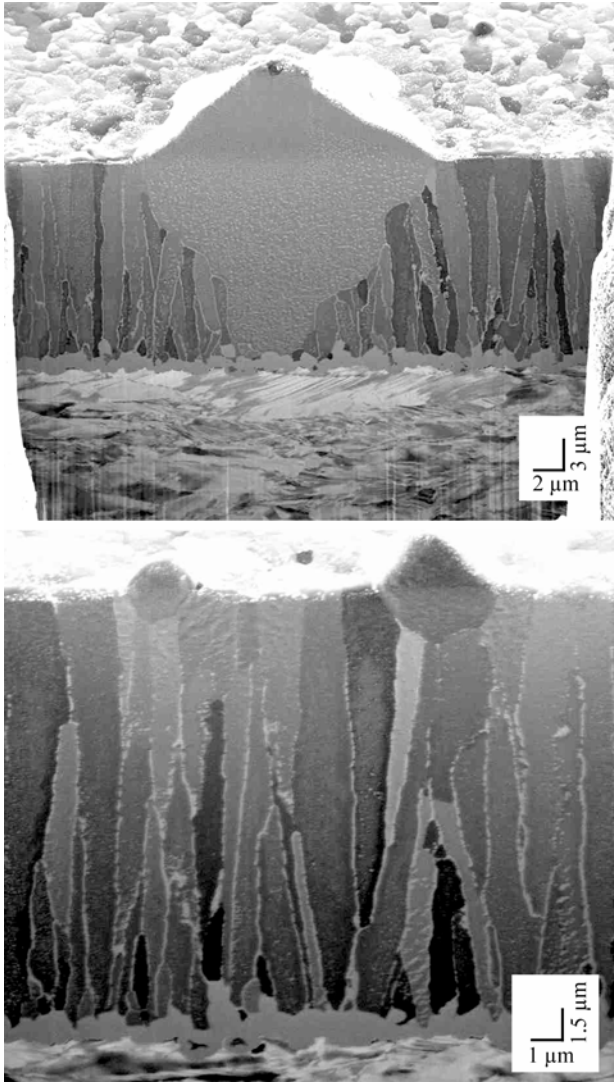


Fig. 3: SEM image of FIBed sample showing small and large hillocks on a 16 μm thick pure Sn electrodeposit. IMC and the bronze are seen at the bottom [04Gal]. The white contrast on the Sn columnar grain boundaries is an artifact of the FIB procedure as is the darker contrast in the hillock grain above the deposit surface.

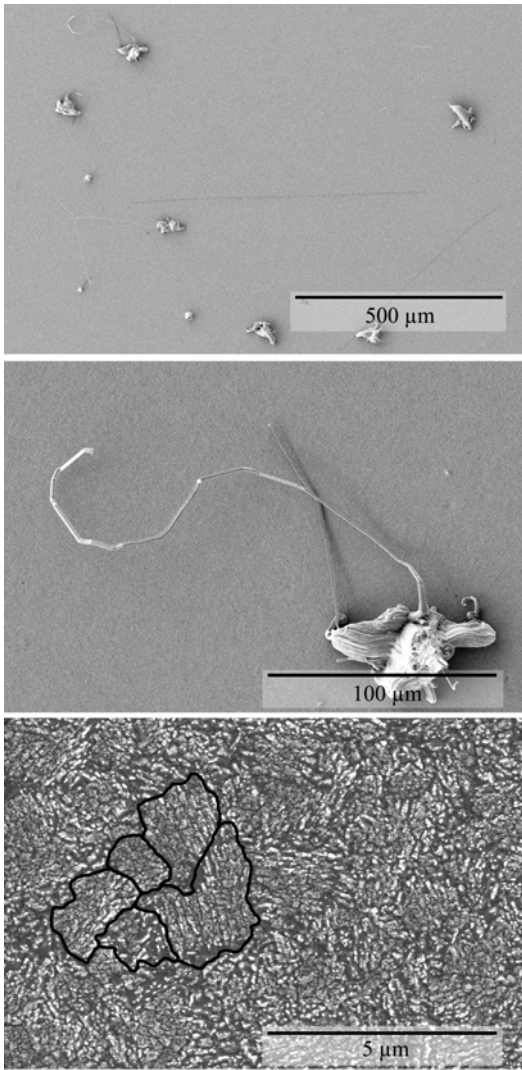


Fig. 4: Low, intermediate and high magnification SEM micrographs of the electrodeposit surface of a 16 μm thick Sn-Cu electrodeposit on a cantilever beam (photo taken after 176 days (1.5×10^7 s)). The fine lines in the top figure are long whiskers. A few Sn grain boundary locations are indicated in the bottom figure.

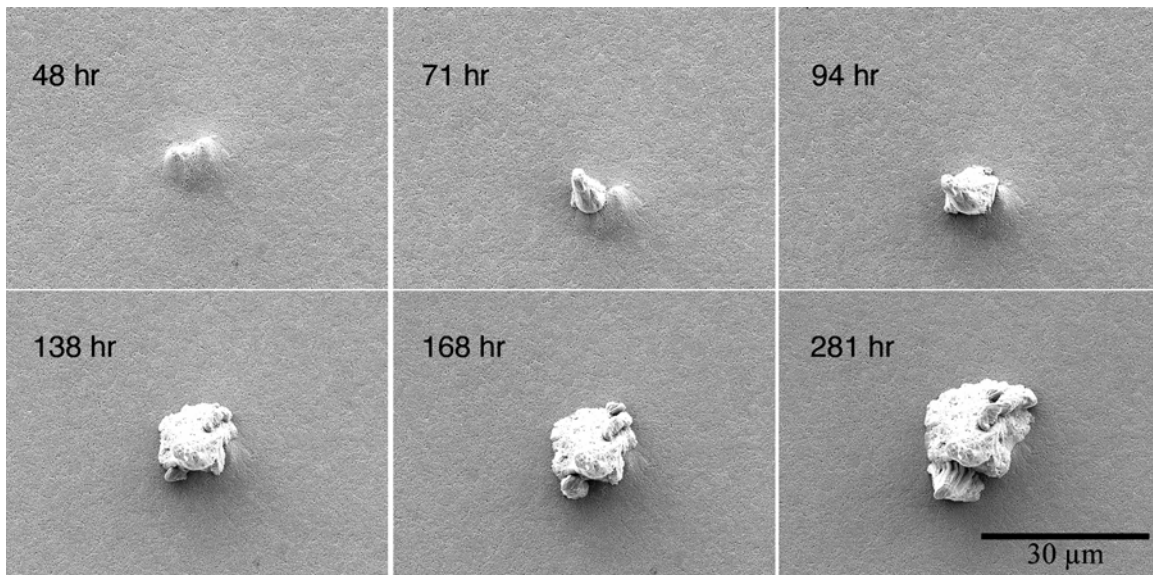


Fig. 5: Time sequence of the formation of an eruption on a Sn-Cu 16 μm thick cantilever sample. Prior to 2 days (1.5×10^5 s) no surface upheaval is observed.

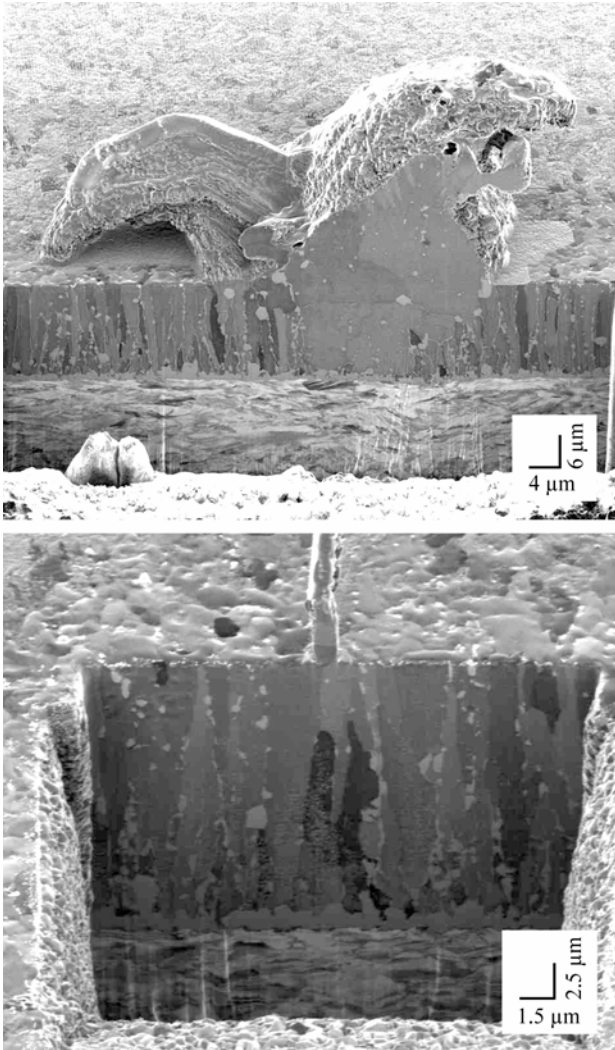


Fig. 6: SEM images of FIBed 16 μm thick Sn-Cu electrodeposit. a) location showing a contorted eruption, b) location showing a filamentary whisker on the same sample. [04Gal].

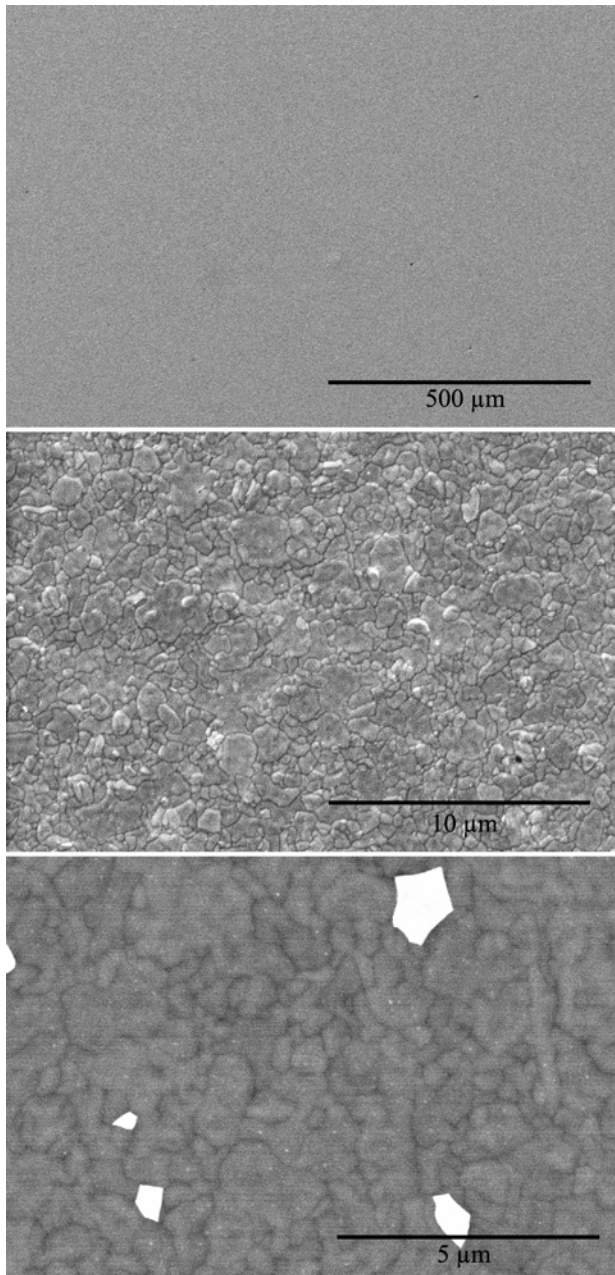


Fig. 7: Low, medium and high magnification SEM micrographs of the electrodeposit surface of a 16 μm thick Sn-Pb electrodeposit on a cantilever beam after 85 days (7.3×10^6 s). The highest magnification SEM micrograph employed back scattered electron contrast and clearly shows four isolated Pb grains.

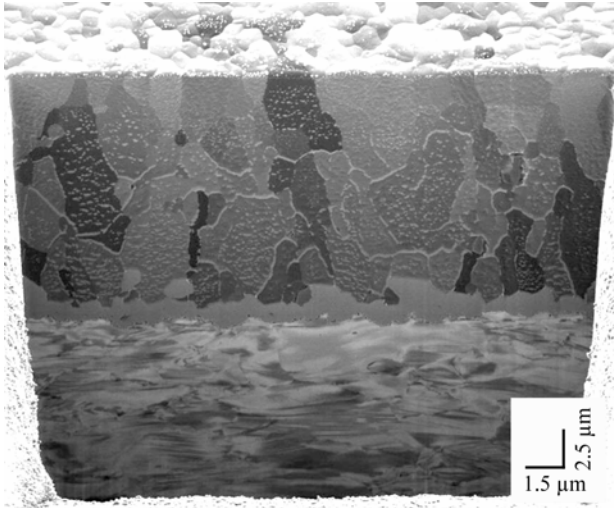


Fig. 8: SEM images of FIBed 16 μm thick Sn-Pb electrodeposit. The grain structure is not columnar. [04Gal].

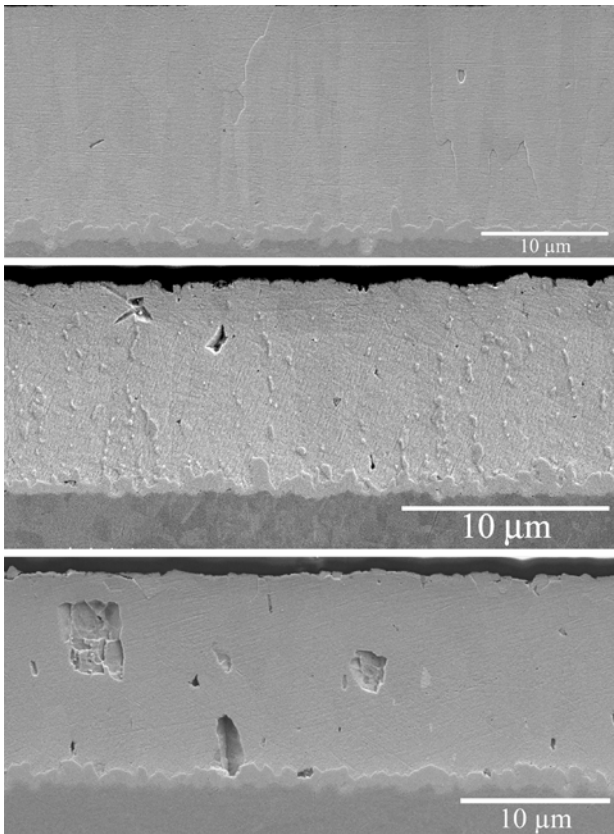


Fig. 9: Cross sections of 16 μm thick (nominal) electrodeposits on phosphor bronze: a) Pure Sn, b) Sn-Cu, c) Sn- Pb approximately one year after plating. The holes in c) are polishing artifacts.



Fig.10: TEM a) bright and b) dark field views of Sn-Cu deposit approximately 24 h after electroplating. Cu_6Sn_5 intermetallic particles were identified by SAD in the interior of the Sn grains and on the grain boundaries. The dark field images show that the internal particles share a common orientation.

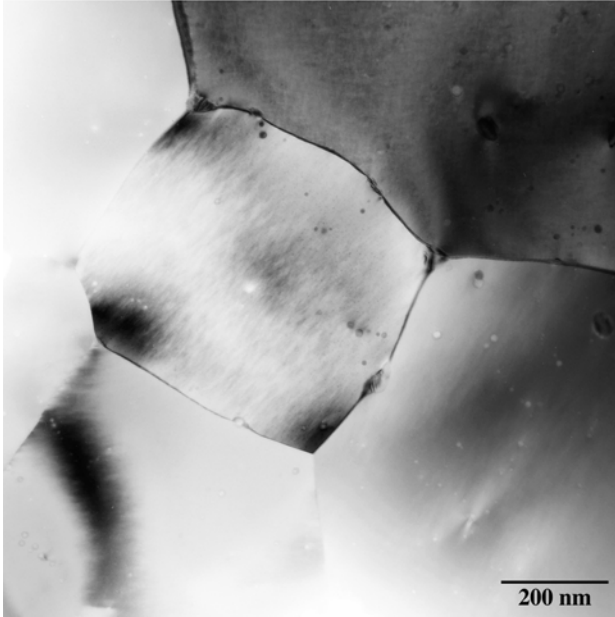
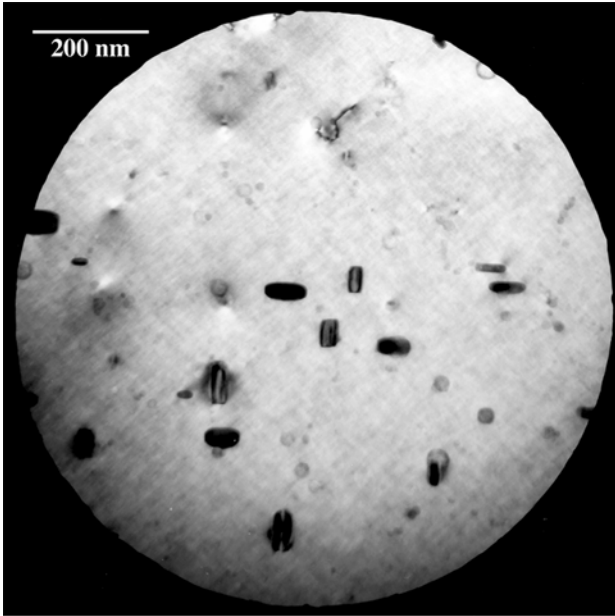


Fig. 11: TEM of Sn Pb-electro deposit one month after plating: a) Pb particles are approximately 50 nm tetragonally distorted cuboids within the Sn grains and b) larger Pb particles on the Sn Grain boundaries.

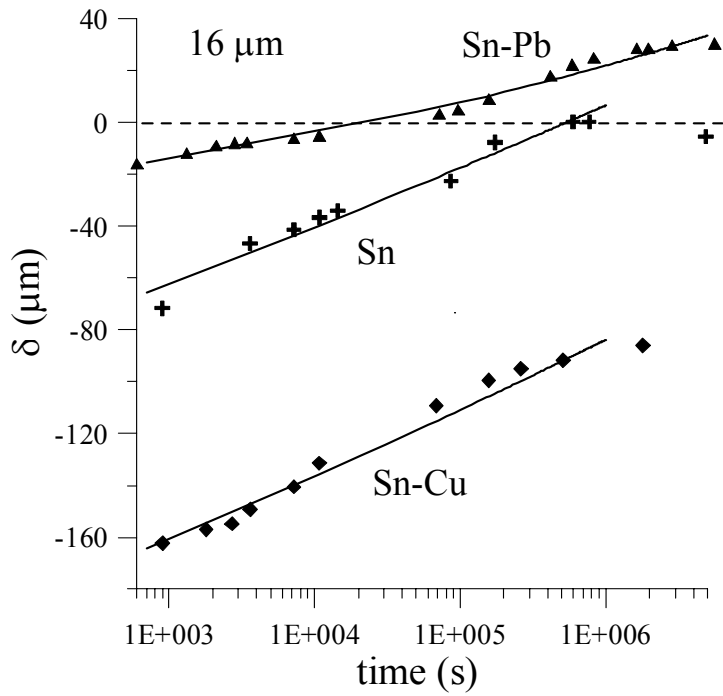


Fig 12a: Deflection vs. time for 16 μm thick deposits. Lines are power law fits.

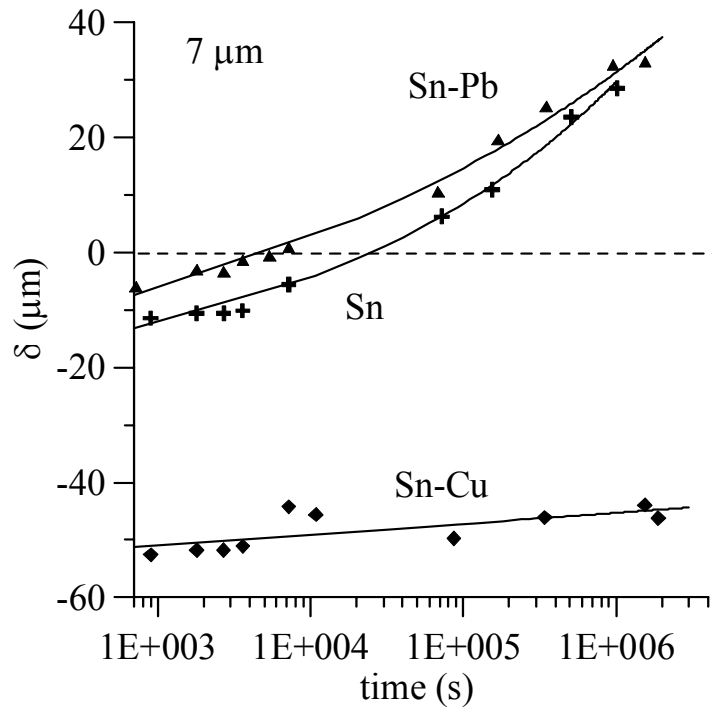


Fig. 12b: Deflection vs. time curves for 7 μm thick deposits. Lines are power law fits.

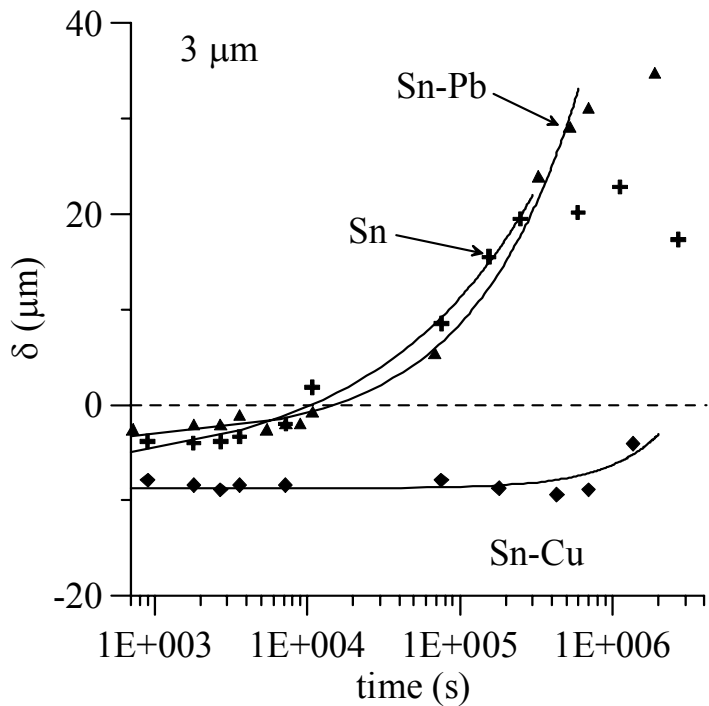


Fig 12c: Deflection vs. time curves for 3 μm thick deposits. Lines are power law fits.

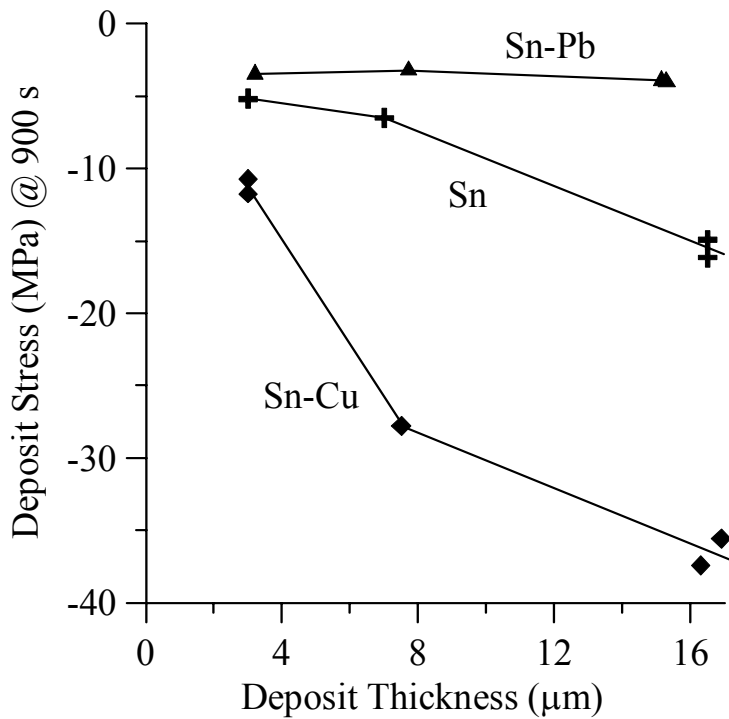


Figure 13: Initial stress (approx. 15 minutes after plating) as a function of plating thickness.

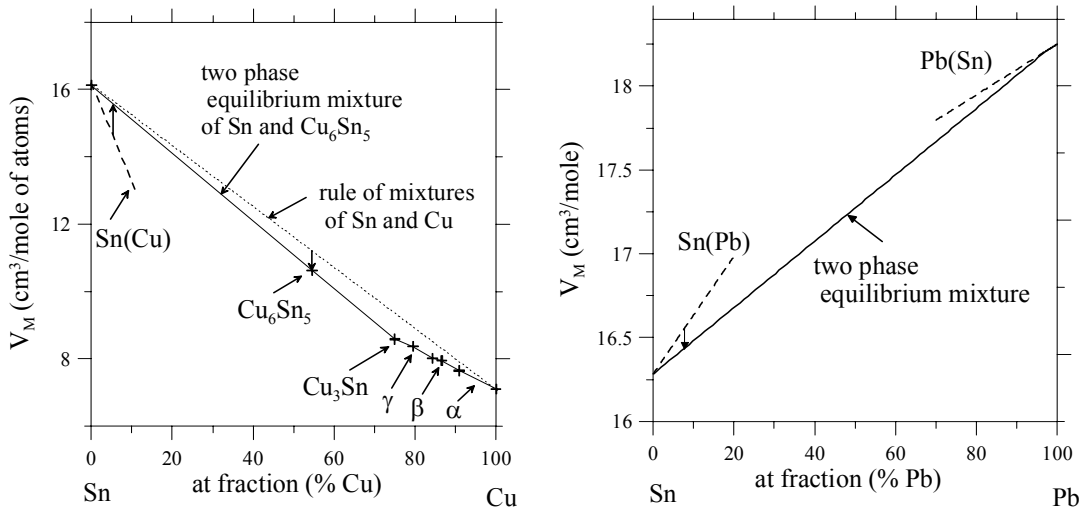


Fig. 14: Volume per mole of atoms for phases for the Sn-Cu and Sn-Pb systems. Dashed lines show supersaturated solid solutions. The vertical arrows show the volume change for the various metallurgical processes.

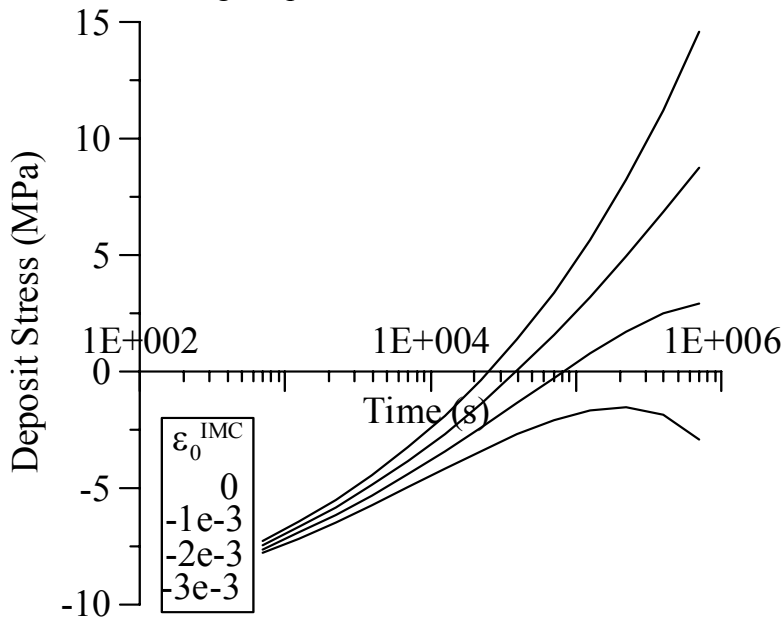


Fig. 15: Deposit stress vs. time extracted from deflection data for pure Sn, 7 μm thick samples. Curves are shown from top to bottom for four different values of the intermetallic stress-free strain, ϵ_{IMC}^0 : 0, -1×10^{-3} , -2×10^{-3} , -3×10^{-3} .

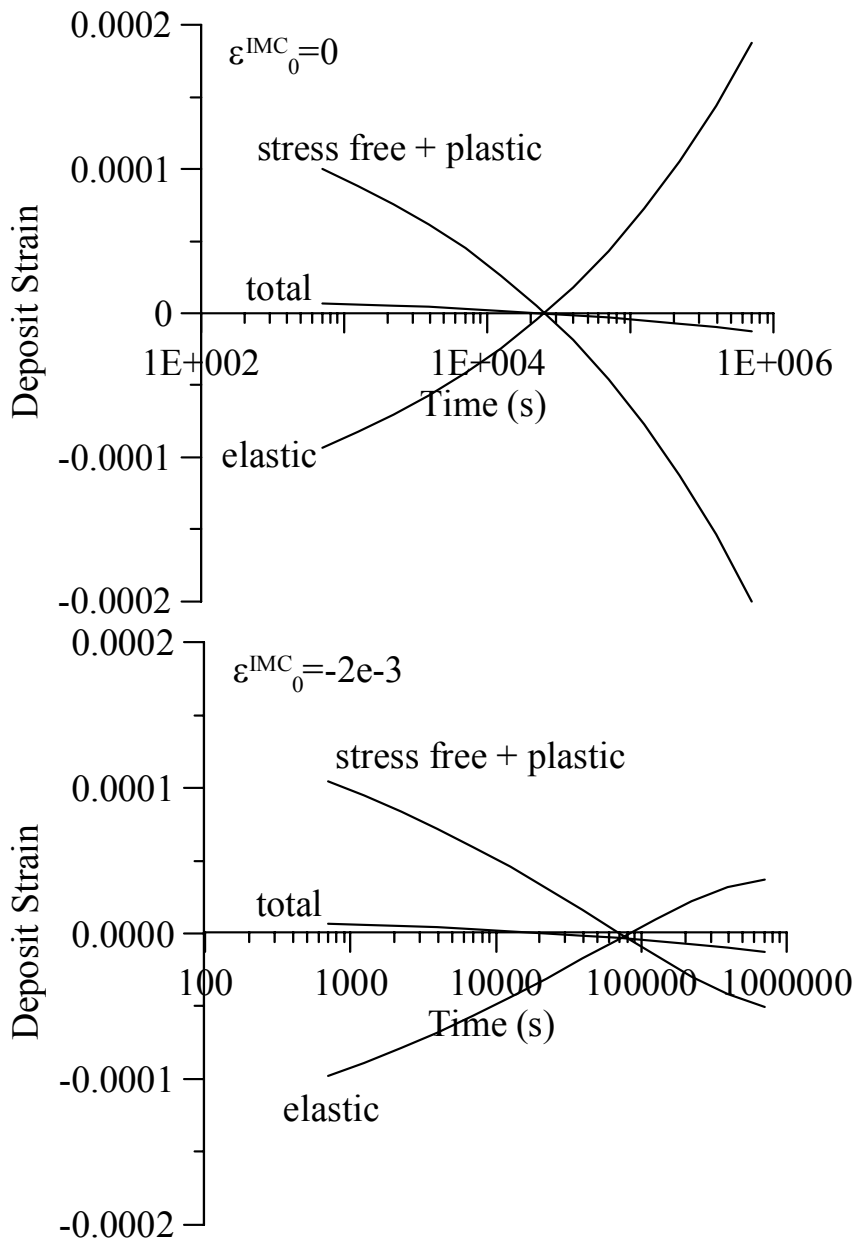


Fig. 16: Total strain, elastic strain and stress free + plastic strain vs. time extracted from deflection data for two assumed values of intermetallic stress-free strain.

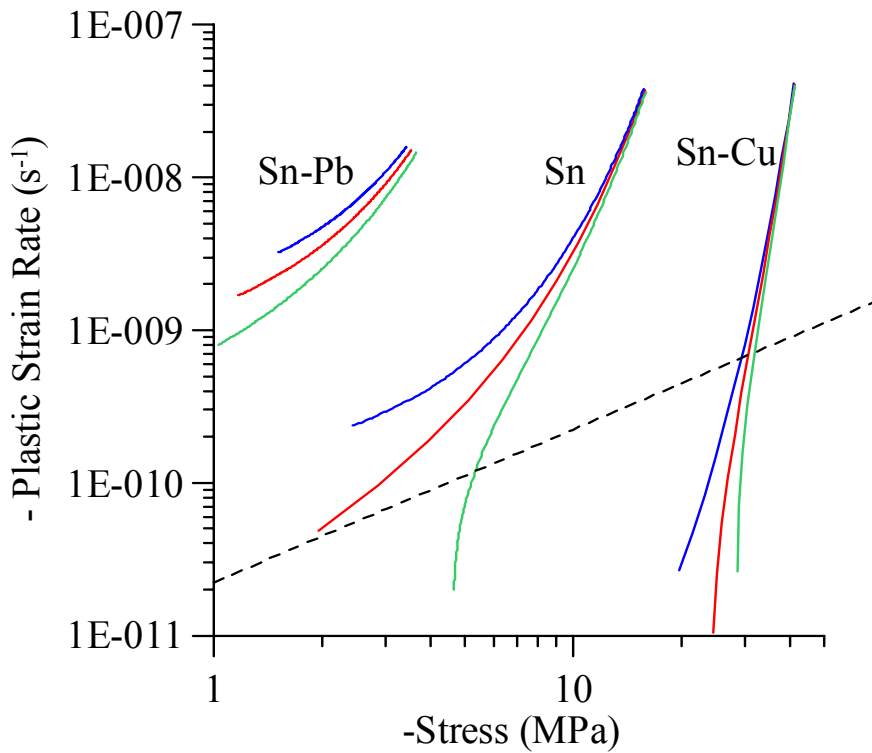


Fig. 17: Log (-plastic strain rate) vs. Log (-stress) for 16 μm thick electrodeposits derived from deflection measurements: Blue, no correction for layer intermetallic stress. Red, corrected for layer intermetallic stress, $\epsilon_0^{IMC} = -0.001$ (stress = 125 MPa tensile). Green, $\epsilon_0^{IMC} = -0.002$ (stress = 250 MPa tensile). The prediction of [04Hut] for whisker growth rate (converted to average strain rate in the in-plane direction) is shown dashed.

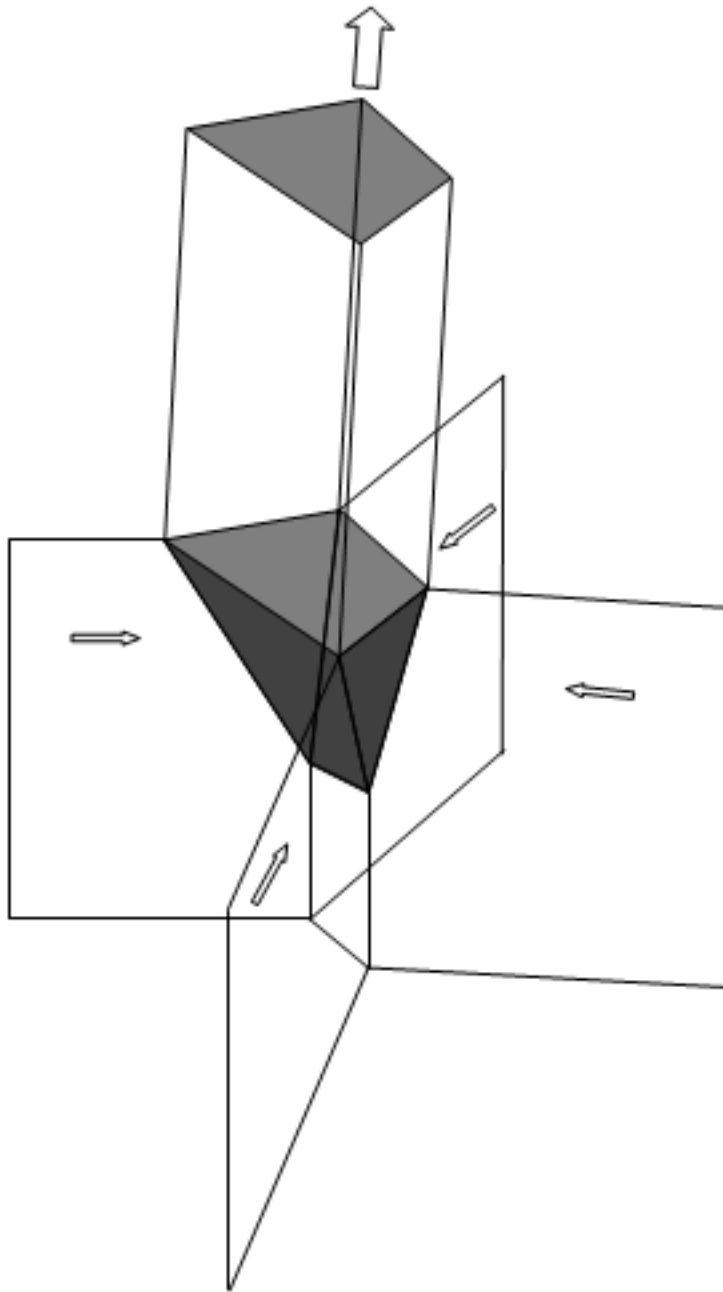


Fig. 18: Region of a deposit near its surface that contains a small grain with interior oblique faces surrounded by columnar grains under bi-axial compressive stress. The three dimensional path of Sn atoms to relieve the stress is along columnar grain faces (arrows) within the deposit, through the triple lines, and across the oblique (black) faces. Accretion of Sn on these faces forces the whisker above the deposit surface.

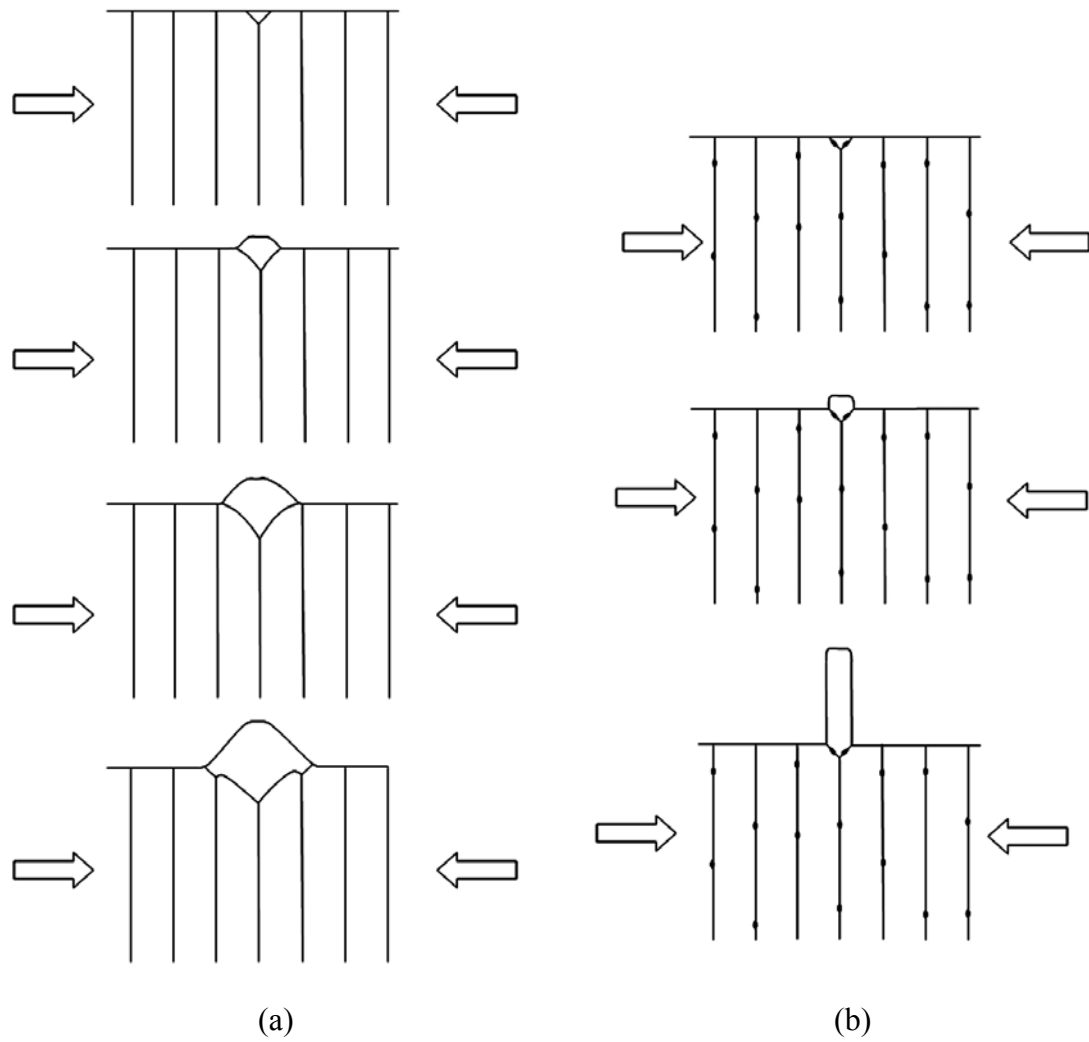


Fig 19: Schematic stress relaxation (creep) by (a) hillock growth and grain boundary migration under a hillock, (b) whisker growth when grain boundaries are pinned by precipitates.